Check for updates

Application of a clustered countercurrent-flow micro-channel reactor in the preparation of KMnF₃ perovskite for asymmetric supercapacitors

Kun-Peng Cheng,[ab] Ren-Jie Gu[ab] and Li-Xiong Wen [ID] *[ab]

A clustered countercurrent-flow micro-channel reactor (C-CFMCR) with adjustable magnification times was constructed for the preparation of KMnF₃ perovskite fluoride by a co-precipitation process, in which the concentrations and feed rates of reactants were precisely controlled. Benefitting from the enhanced micromixing efficiency of the microreactor, the KMnF₃ particles prepared in C-CFMCR were smaller and less aggregated than those produced with traditional stirred reactors (STR). The prepared KMnF₃ was applied as the electrode material in supercapacitors, and the electrochemical measurements showed that the KMnF₃ obtained under optimal conditions had a discharge specific capacitance of ~442 F g⁻¹ at a current density of 1 A g⁻¹, with a decline of ~5.4% after 5000 charge–discharge cycles in an aqueous electrolyte of 2 M KOH. It was also found that the morphologies and electrochemical performances of the prepared KMnF₃ particles changed accordingly with the micromixing efficiencies of C-CFMCR, which can be adjusted by the reactor structure and operating conditions. An asymmetric supercapacitor assembled with the KMnF₃ and activated carbon exhibited an energy density of 13.1 W h kg⁻¹ at a power density of 386.3 W kg⁻¹, with eminent capacitance retention of ~81.2% after 5000 cycles. In addition, only a slight amplification effect of C-CFMCR on the co-precipitation process was noticed, indicating that the C-CFMCR is a promising technology for the massive and controllable production of KMnF₃ particles as well as other ultrafine particles.

1. Introduction

The increasing energy demand together with device miniaturization make it urgent to develop alternative and renewable energy storage resources with fast charge–discharge rate, high cycling stability and low cost. Supercapacitors, which fill the gap between conventional capacitors and batteries, have attracted significantly increasing attention in practical applications ranging from portable electronics and implantable medical devices to electric vehicles.[1–5] There are two accepted mechanisms of charge storage for supercapacitors, *i.e.*, electrical double layer capacitance (EDLC) and pseudo-capacitance.[6] The former, which is developed generally with carbon materials, stores electric energy *via* the accumulation of ions at the electrode/electrolyte interface to generate enormous electric capacity; while for the latter, the energy storage is achieved by fast and reversible faradaic redox reactions taking place in the surface of electroactive materials and the reaction site can provide dozens of times higher energy density in comparison

with the non-faradaic process,[7,8] possessing much larger specific capacitance than EDLCs as a consequence.[9–12]

It is well known that electrode materials play an extremely important role in the performance of supercapacitors. In pursuit of high-performance supercapacitors, suitable electrode materials with high redox activity, good conductivity and electrical stability must be developed. Various forms of carbonaceous materials, transition metal compounds and conducting polymers have been investigated and used extensively as electrode materials for supercapacitors.[13–18] Perovskite-type materials with the nominal formula of ABC₃, where A is a lanthanide or alkali earth element and B is a valence-variable metal cation, have been widely studied as electrodes for solid fuel cells and supercapacitors on account of their inherent 3D diffusion channels and robust structure with intersectant orthogonal cavity chains.[19–23] Because of the considerable ionic essence of transition metal-fluoride bonds and inherent high rate of ion diffusion, perovskite fluorides have been considered as a promising candidate to replace perovskite oxides for electrochemical applications.[24,25] It has been reported that KCoF₃ demonstrates good electrochemical stability and energy storage capacity.[26] KMnF₃ is a manganese-containing fluoride with perovskite-type structure and improved conductivity. In addition, evidences show that there exist inherent cation vacancies in Mn-contained compounds in terms of ions intercalation in

aResearch Center of the Ministry of Education for High Gravity Engineering and Technology, Beijing University of Chemical Technology, Beijing 100029, China. E-mail: wenlx@mail.buct.edu.cn

bCollege of Chemical Engineering, Beijing University of Chemical Technology, Beijing 100029, China

charge–discharge process,[27,28] which can be exploited to improve charge storage through the insertion of electrolyte cations into Mn vacancies. However, little research on perovskite fluorides for electrode materials of supercapacitors has been conducted.

There are several methods for the synthesis of perovskite fluorides, such as hydrothermal,[29] inverse micelle method,[30] reaction precipitation[31] and horizontal Bridgman method.[32] Compared to reaction precipitation, other methods suffer several drawbacks, such as inflexible process, environmental unfriendly and large space occupation for peculiar devices. Besides, the low throughput could hardly satisfy the demands of commercialization.

Precipitation is a flexible process for the synthesis of particles with varying morphologies and other specified properties, in which uniform and high level of supersaturation is essential because of the highly nonlinear dependency of the nucleation rate on supersaturation.[33] Since precipitation processes are generally accompanied by very fast reactions, rapid micromixing is desired to generate uniform level of supersaturation and promote the product quality consequently. However, high micromixing efficiency is hard to be achieved in conventional stirred reactor (STR) due to the inhomogeneous local distribution of concentration and flow rate, leading to uneven element distribution within the prepared material. To address above disadvantages, many microstructured devices for process intensification, such as confined impinging jet reactor,[34] Y-type microchannel reactor,[35] microporous tube-in-tube microchannel reactor,[36] rotor–stator mixer,[37] *etc.*, have been developed for performing chemical reaction and separation processes, in which fast micromixing is desired. All these precisely designed devices can remarkably strengthen micromixing performance and provide an even environment for energy dissipation and reactants distribution. Nevertheless, most of the micromixing-intensified instruments are either difficult to be manufactured and scaled up by reasons of their complex structures or vulnerable to severe blocking problem and low yield limitation when it comes to practical applications. In this regards, development of new micromixing-enhanced devices with advantages of simple configuration, ease to scale up and slight blocking remains an urgent challenge for chemical precipitation processes.

For this purpose, we built a clustered countercurrent-flow micro-channel reactor (C-CFMCR) by numbering-up its single counterpart, *i.e.*, a single countercurrent-flow micro-channel reactor (S-CFMCR), and studied its micromixing performance (expressed as micromixing time, t_m) experimentally.[38] It was found that C-CFMCR had notable advantages of strengthening micromixing, easy to be fabricated, flexible operation in continuous manner and easy to be scaled up with controllable magnification times. Hence it was expected to be an efficient technology for the massive precipitation of nanoparticles or ultrafine particles. In this work, C-CFMCRs were applied to prepare ultrafine $KMnF_3$ particles with varying feed rate and were compared to the same product synthesized in STR. The amplification effect of the as-developed reactor was explored by assembling C-CFMCRs with different number of S-CFMCR. In addition, the electrochemical properties of $KMnF_3$ in a three-electrode system as well as a practical application as supercapacitor were assessed.

2. Experimental

2.1. Chemicals and reagents

Potassium fluoride dihydrate ($KF \cdot 2H_2O$) and manganese chloride tetrahydrate ($MnCl_2 \cdot 4H_2O$) were obtained from Guangfu Fine Chemical Factory (Tianjin, China). Acetylene black, polyvinylidene fluoride (PVDF), and *n*-methyl-2-pyrrolidinone (NMP) were provided by Sinopharm Chemical Reagent Co., Ltd. (China). Potassium hydroxide (KOH) was purchased from Tongguang Fine Chemical Ltd. (Beijing, China). Activated carbon (AC) (with a specific surface area of 1600 m^2 g^{-1}) was obtained from Kuraray China Co., Ltd. (Shanghai, China). All
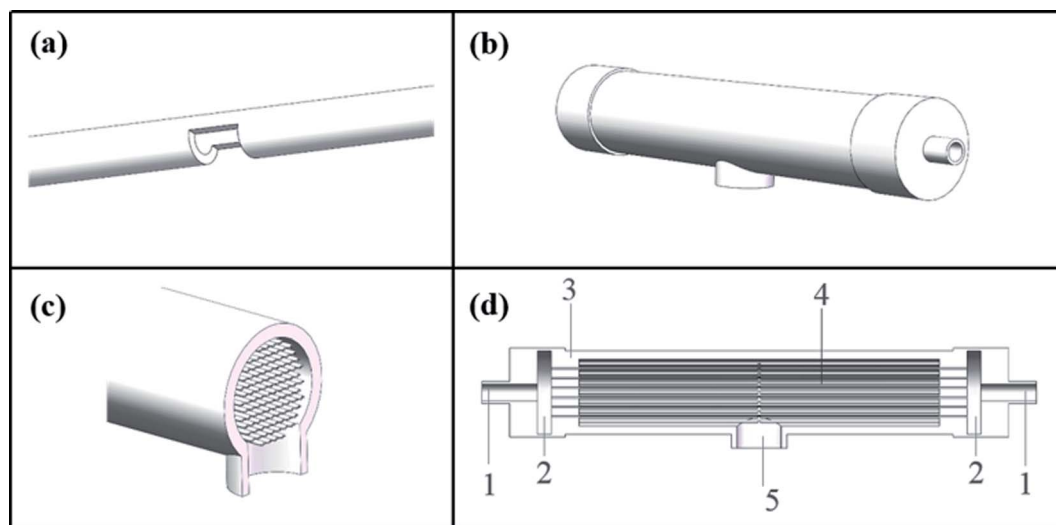

Fig. 1 Structure of assembled C–CFMCR: (a) S-CFMCR, (b) outer appearance of C-CFMCR, (c) middle cross-section of C-CFMCR, (d) front cross-section of C-CFMCR: (1) main inlet; (2) buffer zone; (3) shell; (4) S-CFMCRs; (5) main outlet.

Table 1 Operation conditions for the synthesis of KMnF₃ in S-CFMCR and C-CFMCR

| Ref.	Volumetric flow rate (mL min⁻¹)	Incoming flow velocity (m s⁻¹)	Number of S-CFMCR	Micromixing time t_m (ms)[38]
KMF01	20	1.18	1	1.75
KMF02	40	2.36	1	0.34
KMF03	60	3.54	1	2.07
KMF04	80	4.72	1	4.35
KMF05	200	2.36	5	0.61
KMF06	400	2.36	10	0.76
KMF07	—	—	STR	20 (ref. 39)

chemicals were of analytical grade and used without further purification.

2.2. Construction of C-CFMCR

The C-CFMCR (Fig. 1b–d) was integrated by its counterpart S-CFMCR (Fig. 1a) as stated in our previous work,[38] which possesses the advantages of easy to fabricate, flexible operation and variable magnification factors.

2.3. Synthesis of KMnF₃

The co-precipitation processes of KMnF₃ were carried out at ambient temperature. A 0.6 M KF·2H₂O solution and a 0.2 M MnCl₂·4H₂O solution were introduced into C-CFMCR simultaneously from the two main inlets by precise plunger pumps or directly mixed by vigorously stirring in STR, generating KMnF₃ according to the following equation:

$$3KF \cdot 2H_2O + MnCl_2 \cdot 4H_2O \rightarrow KMnF_3 + 2KCl + 6H_2O \quad (1)$$
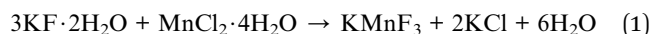
The volumetric flow ratio of the two injecting streams was kept at 1 for coaxially balanced convection at the exit zone with varying volumetric flow rate ranging from 10 to 80 mL min⁻¹ (corresponding to a Reynolds number varying from 394 to 3152 with an inlet diameter of 0.6 mm) in each individual S-CFMCR. The collected suspension was stirred at room temperature for 4 h and then washed with deionized water and ethanol for several times, and dried in a vacuum oven overnight at 60 °C to obtain white powders. The precipitation conditions are illustrated in Table 1, in which the micromixing time is determined by the liquid flow rate within the specific reactors.

2.4. Material characterization

The crystal structure of samples was analyzed using X-ray diffraction (XRD, Bucker D8, Germany), applying Cu Kα radiation (λ = 0.1542 nm) as the source from 10 to 80° with a scan rate of 10° min⁻¹. The optical absorption measurement was carried out by using UV-VIS-NIR spectrophotometer (Shimadzu UV-3600, Japan) from 800 to 220 nm. Energy dispersive spectroscopy (EDS) and morphology analyses were conducted with a scanning electron microscopy (SEM, JEOL S-7800, Japan). The surface electronic states were captured by X-ray photoelectron spectra (XPS, ESCALAB-250, USA) with Al Kα radiation. N₂ absorption

desorption isotherm was recorded by an ASAP 2010 instrument (Micromeritics, USA) after pretreated in vacuum for 6 h.

2.5. Electrode preparation and electrochemical characterization

The working electrode was prepared by mixing the active material KMnF₃, acetylene black and polyvinylidene fluoride (PVDF) with a mass ratio of 8 : 1 : 1, a proper amount of *n*-methyl-2-pyrrolidinone (NMP) was then added into the mixture. A nickel foam substrate (1 × 1 × 0.1 cm) was coated with the above-obtained slurry, dried at 80 °C for 12 h and pressed under 10 MPa into a thin wafer. The mass loading of active material was 1.5–2.5 mg cm⁻².

Electrochemical tests were conducted in a three-electrode system by an electrochemical workstation (CHI660E, CH Instruments Inc., USA), with a platinum plate and an Hg/HgO electrode employed as the counter and reference electrode, respectively. 2 M KOH aqueous solution was used as the electrolyte. A few cyclic voltammetry (CV) cycles were carried out in advance to activate the electrode, followed by galvanostatic charge–discharge (GCD) and cyclic voltammetry (CV) tests. The electrochemical impedance spectroscopy (EIS) measurement was conducted in the frequency range from 100 kHz to 10 mHz at 0 V (*vs.* open circuit). The cycling performance were measured by a GCD equipment (LANHE CT2001A, Wuhan LAND, China). The specific capacitance (*C*, F g⁻¹) was obtained from galvanostatic discharge measurement by the following equation:

$$C = \frac{I\Delta t}{m\Delta V} \quad (2)$$

where I (A), Δt (s), ΔV (V) and m (g) are constant discharge current, discharge time, voltage window and the mass of active material, respectively.

The coin-cell asymmetric supercapacitors (ASC) were assembled by using KMnF₃ particles as positive electrode and activated carbon (AC) as negative electrode in 2 M KOH aqueous solution with nonwoven fabric as separator. The negative electrode was prepared using the same method as used for the positive electrode. The mass ratio between the positive and negative electrodes of ASC for achieving charge balance was expressed as the following equation:

$$\frac{m_+}{m_-} = \frac{C_-\Delta V_-}{C_+\Delta V_+} \quad (3)$$

where m_+/m_-, C_+/C_-, and $\Delta V_+/\Delta V_-$ denote the masses, specific capacitances and potential window upon discharging for the positive and negative electrodes, respectively.

The energy density (E, W h kg⁻¹) and power density (P, W kg⁻¹) were calculated using the following formulas:[40]

$$E = \frac{C_{cell} V^2}{2 \times 3.6} \quad (4)$$

$$P = \frac{3600E}{\Delta t} \quad (5)$$

where C_{cell} denotes the specific capacitance of assembled ASC obtained based on the total mass of activated material in both

positive and negative electrodes, V and Δt are the specified potential window and discharge time, respectively.

3. Results and discussion

3.1. Characterization of structure and morphology

$KMnF_3$ particles were synthesized in STR, one S-CFMCR and two C-CFMCRs with different magnification times (*i.e.*, 5 and 10 times), respectively, under varying fluid flow rates, and their XRD patterns are demonstrated in Fig. 2a. All the diffraction peaks in each individual profile can be perfectly attributed to cubic pervoskite structure $KMnF_3$ (JCPDS 84-0442) with space group of $Pm\bar{3}m$. There was no significant distinction in XRD patterns for the $KMnF_3$ samples prepared in S-CFMCR (labeled as KMF02, refer to Table 1) and in the integrated C-CFMCR with different magnification factors (KMF05 and KMF06), in which the highly crystalline nature of the materials were all confirmed. However, broadening and weaker peaks were observed for the

sample prepared in STR in comparison to that prepared in microreactor-route, suggesting much poorer crystallinity for the STR sample. The textural properties and porosity of the KMF02 and KMF06 were evaluated by N_2 absorption/desorption isotherms and pore size distributions. As illustrated in Fig. 2b, both samples showed typical type-IV isotherms with small hysteresis loop at relative pressure $P/P_0 = 0.2$–1.0, revealing the existence of mesopores within them.[41] Both precipitates exhibited narrow pore size distribution profiles with a maximum between 2 to 8 nm, which might be originated from the interspace among the aggregated particles (Fig. 3). The calculated BET surface area of KMF02 and KMF06 were 10.8 and 9.7 m² g⁻¹, respectively. Fig. 2c displays the UV-Vis absorption spectrum of $KMnF_3$, indicating that $KMnF_3$ absorbs light with wavelength shorter than 580 nm. The optical band gap of $KMnF_3$ was estimated to be 3.04 eV by extrapolating the plot of $(Ah\nu)^2$ *versus* photon energy ($h\nu$) (Fig. 2d) as proposed in pervious research.[42,43]
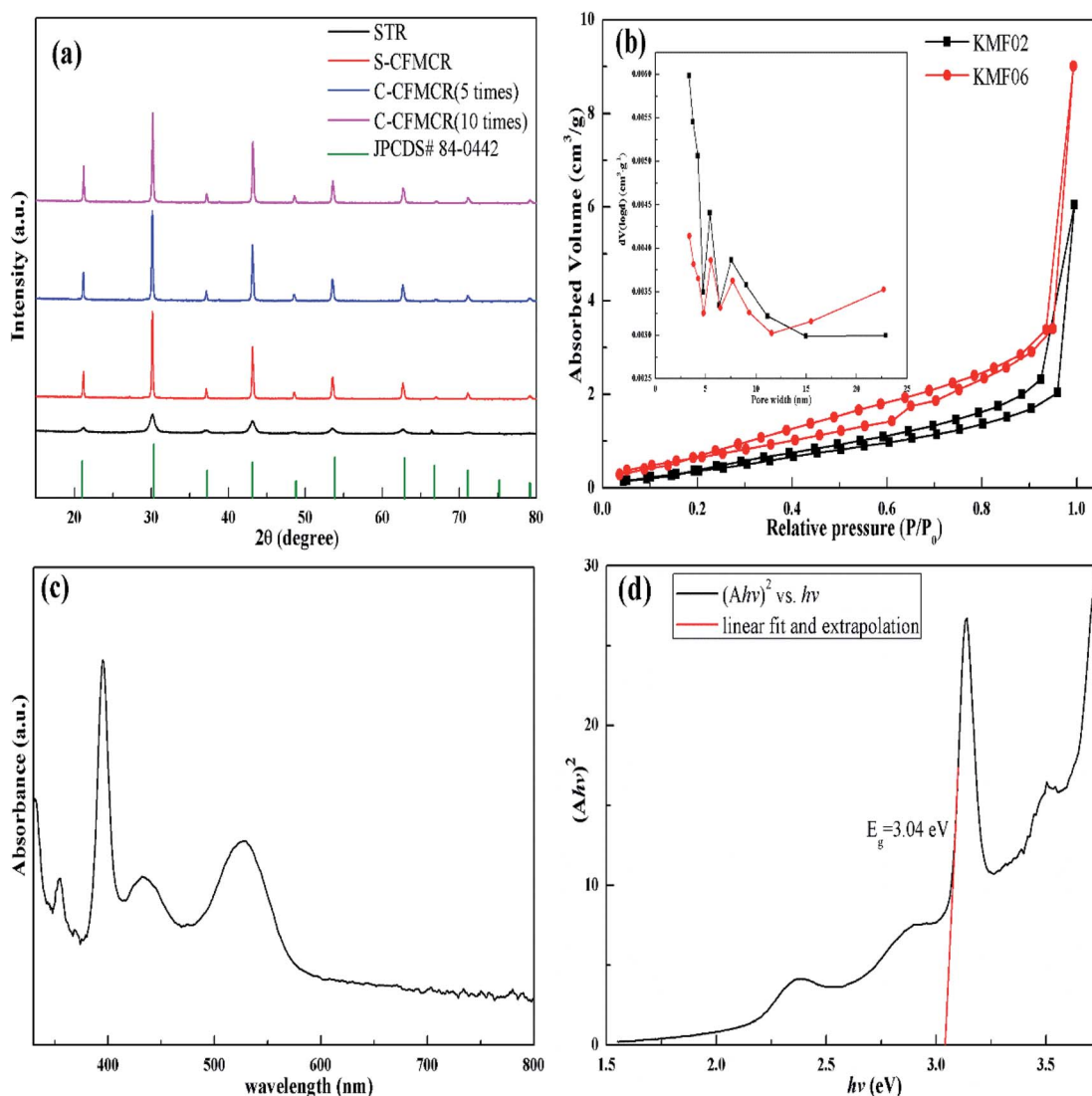

Fig. 2 Structure characterization: (a) XRD patterns, (b) N_2 absorption/desorption (inset is pore size distributions) of different samples, (c) UV-Vis absorption spectrum and (d) corresponding $(Ah\nu)^2$ *vs.* energy ($h\nu$) curve of a $KMnF_3$ film.
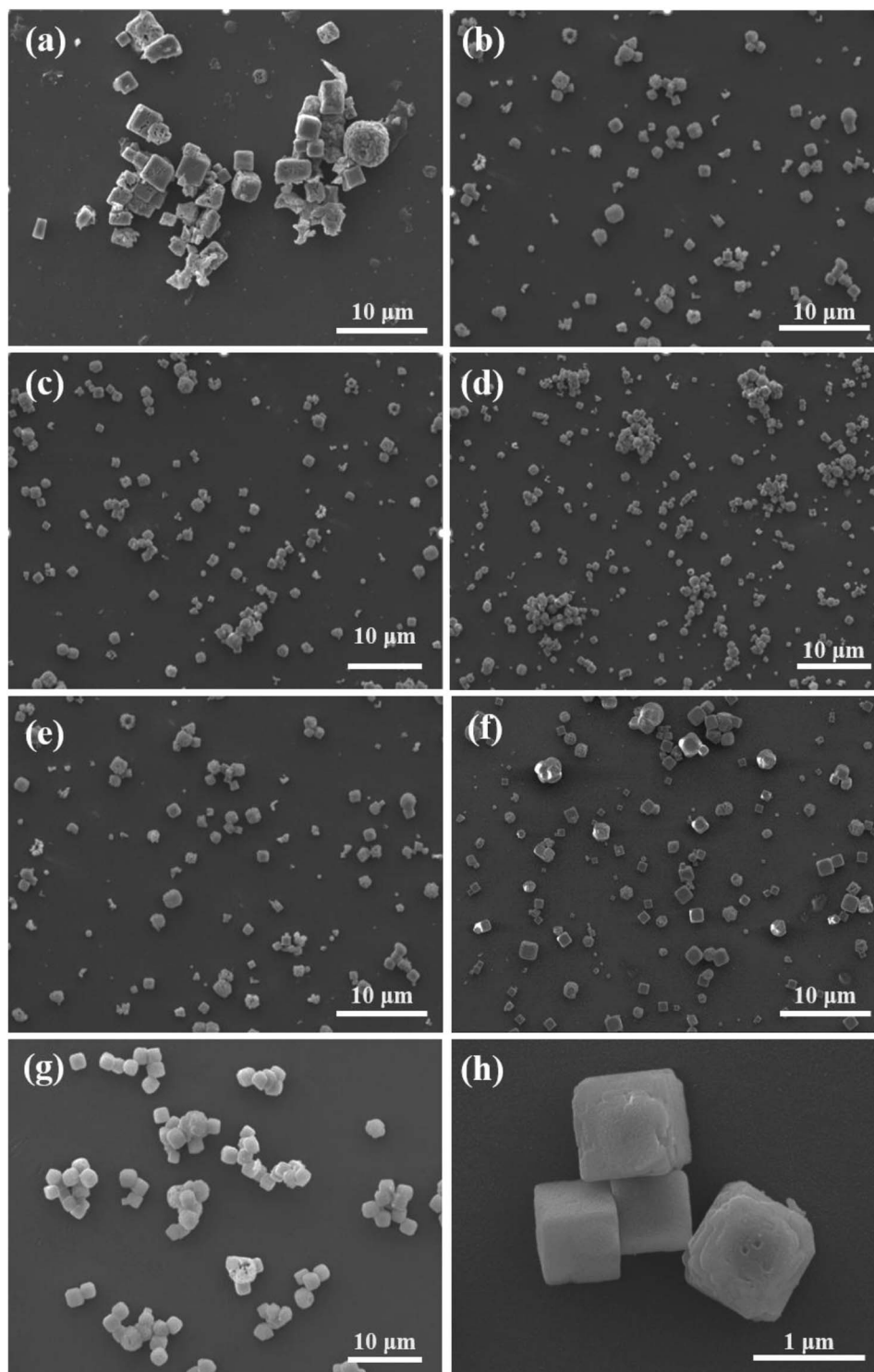
Fig. 3 SEM images of KMnF$_3$ particles prepared under different operating conditions: (a) KMF01, (b) KMF02, (c) KMF03, (d) KMF04, (e) KMF05, (f) KMF06, (g) KMF07 and (h) KMF02 under high resolution.

The different reactors under varying operating conditions have different micromixing time t_m (Table 1). Fig. 3 presents the SEM images of KMnF$_3$ particles prepared under different conditions. The KMnF$_3$ particles produced in S-CFMCR at a volumetric flow rate of 20 mL min^{-1} (Re = 788, Fig. 3a) had

low crystallinity and incomplete growth of structure with relatively large size distribution. Along with the increasing volumetric flow rate (Fig. 3b–d), the obtained KMnF$_3$ particles exhibited smaller and more uniform morphologies but different degree of agglomerations was observed at larger
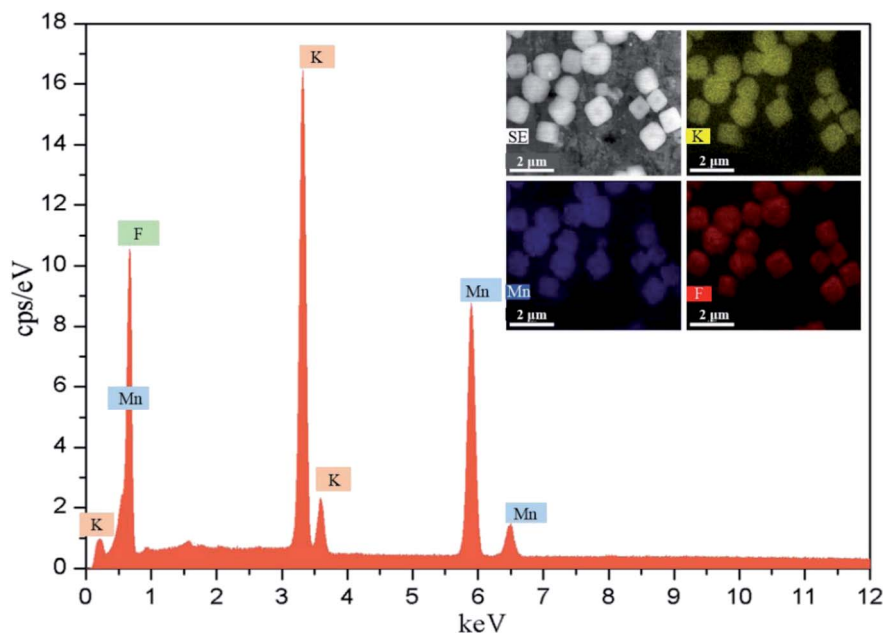
Fig. 4 EDX spectrum with mapping of KMF02.

micromixing time scale (Fig. 3c and d). In accordance with the effect of operating parameters on the micromixing time of S-CFMCR (see Table 1), promoted morphology of precipitated $KMnF_3$ particles was achieved under intensified micromixing performance (*i.e.*, shorter micromixing time). The optimal volumetric flow rate for the precipitation of $KMnF_3$ was found to be 40 mL min^{-1} in one single S-CFMCR, which showed the best micromixing efficiency at the same time. The strengthened micromixing performance would lead to higher level of supersaturation and more homogeneous distribution of dissipated energy, which would favor nucleation rather than growth process and consequently result in smaller and more uniform particles. The KMF02, KMF05 and KMF06 samples prepared in S-CFMCR, 5-times integrated C-CFMCR and 10-times integrated C-CFMCR, respectively, demonstrated similar morphology and insignificant agglomeration with uniform size of ∼1 μm (Fig. 3b, e and f), which were associated with their close micromixing time (Table 1) and also revealed the weak amplification effect from S-CFMCR to C-CFMCR. The precipitates prepared in STR (Fig. 3g) showed a slightly larger particle size and more severe aggregation in comparison with that prepared in S-CFMCR (Fig. 3b). That might be due to the different types of precipitation and micromixing behaviors between the two routes. During STR operations, the already generated precipitates remained in the stirred reactor throughout the whole process and kept contacting with the mother liquid, the freshly added reactants as well as newly formed particles. Therefore, the growth period of all particles in STR experienced a wide range of residence time, leading to the uneven size distribution as a consequence. By contrast, the residence time within the S-CFMCR was very short and the whole precipitation process was completed quickly under specified operating condition with desired micromixing performance. All the precipitates

possessed almost the same residence time, local concentration, turbulent kinetic energy and same level of supersaturation, thus more uniform products were obtained in S-CFMCR and C-CFMCR. Fig. 3h displays clearly a cubic structure of the precipitates by SEM analysis with higher resolution, which agreed well with the XRD data. The EDX analysis with element distributions is illustrated in Fig. 4. There are no impurity peaks being observed, indicating high purity of the as-prepared samples.

3.2. Electrochemical characterization

The electrochemical behavior of KMF02 electrode material, which was prepared under the quickest micromixing in S-CFMCR and of improved morphology, was studied utilizing a typical three-electrode electrochemical system with 2 M KOH electrolyte. Fig. 5a gives the CV measurement curves over varying scanning rate (*vs.* Hg/HgO). As observed, the $KMnF_3$ displayed a conspicuous characteristic of faradaic pseudocapacitor with a pair of distinct redox peaks. With the scanning rate increasing from 10 to 100 mV s^{-1} over a voltage of 0–0.6 V, the CV curves possessed similar shape, in which the positions of oxidation and reduction peaks shifted positively and negatively, respectively, revealing an excellent capacitive performance and quasi-reversibility of redox reactions on electrode.[44]

Fig. 5b depicts the discharge curves of KMF02 recorded at different current densities, in which a distinct discharge voltage plateau around 0.3 V and a less dramatic discharge voltage plateau around 0.45 V can be observed. These voltage plateaus can be indexed to the cathodic peaks presented in Fig. 5a, which indicates that the charge–discharge processes of $KMnF_3$ are primarily attributed to faradaic redox reactions and contribute to an outstanding capacitance nature as a result. The cathodic and anodic peaks in the CV curves can be attributed to faradaic
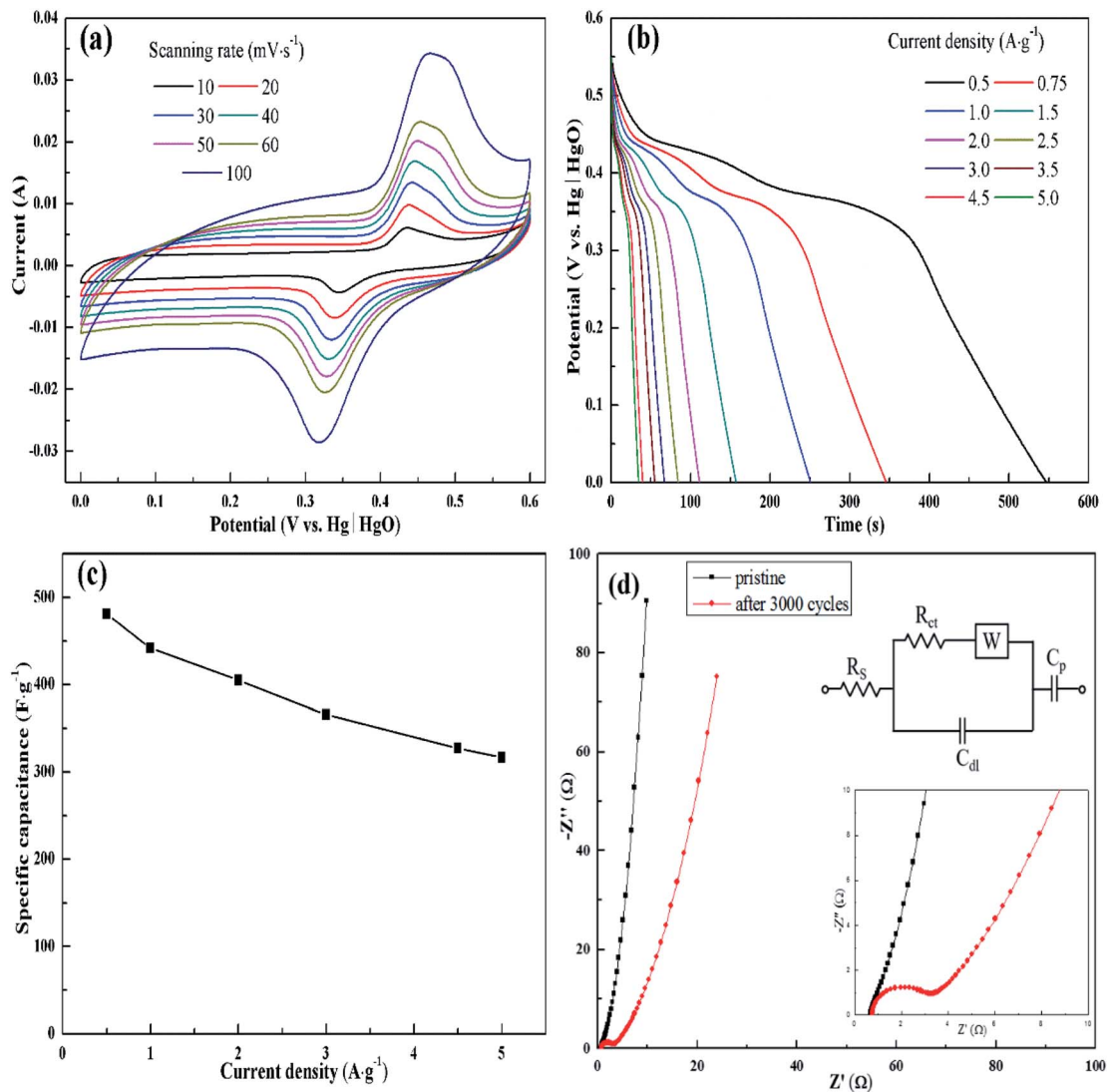
Fig. 5 Electrochemical characterization of KMF02: (a) CV curves at different scan rates, (b) GCD curves at different current densities, (c) specific capacitances at different current densities, (d) Nyquist plots of EIS before and after 3000 cycles (inset is equivalent circuit diagram).

redox reaction of $Mn^{2+}/Mn^{3+}/Mn^{4+}$ in KOH solution. The corresponding specific capacitances calculated from eqn (2) are given in Fig. 5c, in which the $KMnF_3$ electrode exhibited a specific capacitance of 481, 442, 405.1, 365.6, 327.3 and 316.5 F g^{-1} at a current density of 0.5, 1, 2, 3, 4.5 and 5 A g^{-1}, respectively, indicating a high rate capability. The capacitance of $KMnF_3$ outperforms most similar materials, such as $SrMnO_3$,[23] $LaMnO_3$ (ref. 45) and $BaMnF_4$.[29]

The EIS spectra corresponding to the as-prepared $KMnF_3$ electrode and cycled electrode, for characterizing its impedance behavior, are shown in Fig. 5d. The high frequency intersection with X axis denotes the internal resistance (R_s), including the ionic resistance of electrolyte, inherent resistance of active material, and the contact resistance between active material and electrolyte.[46] The R_s of the KMF02 electrode material as-prepared and after 3000 cycles were 0.67 and 0.75 Ω, respectively. The low R_s of $KMnF_3$ electrode material indicates its excellent diffusion ability. The diameter of the semicircle

showed in the higher frequency implies the charge transfer resistance (R_{ct}) of the redox reaction at the electrode/electrolyte interface. It could be noticed that the simulated R_{ct} of KMF02 electrode material increased significantly (from 0.27 to 2.23 Ω) after 3000 charge–discharge cycles, which might be ascribed to the partial exfoliation of active materials from the substrate during the long charge–discharge process.

The electrochemical properties of $KMnF_3$ obtained under various operating parameters were also assessed by GCD measurement at a current density of 1 A g^{-1}. The change of specific capacitance with micromixing time is illustrated in Fig. 6a. Overall, decreasing micromixing time would improve the specific capacitance. In accordance with the effects of micromixing time on the morphology of the prepared particles, KMF02, KMF05 and KMF06, which were synthesized with close micromixing time and the same volumetric flow rate in each individual channel (40 mL min^{-1}), showed similar specific capacitances, indicating a negligible amplification effect from

S-CFMCR to C-CFMCR. It is well known that the electrochemical performances of electrode material are greatly determined by its particle size and degree of agglomeration, which are strongly affected by the micromixing efficiency as well as the level of supersaturation during the preparation process. It was found that the specific capacitances of electrode materials precipitated either at low volumetric flow rate (KMF01) or at high volumetric flow rate (KMF03 and KMF04) were relatively low. Such phenomenon was caused by the mixing characteristics of S-CFMCR, in which the mixing behavior occurrs primarily in the convection zone of the two injected fluids. As the feed rate was too low, the flow of the two fluids was too weak to collide with each other and might flow out of the exit from their respective side, leading to poor micromixing and uneven distribution of energy dissipation. On the other hand, if the feed rate was too high, the injected streams would impact strongly and part of the reactants would sputter out without mixing with each other due to the unconfined exit of the reactor, which also resulted in a low micromixing performance as well as waste of energy. In addition, the poor performance of KMF01 in specific capacitance may also be ascribed to its anomalous morphology (Fig. 3a). Thus, an appropriate injecting volumetric flow rate must be selected to assure not only fast micromixing but also enough momentum acted on the buffer zone (Fig. 1d) to achieve uniform distribution of fluids into the assembled S-CFMCRs and weaken the magnification effect consequently. Therefore, a volumetric flow rate of 40 mL min^{-1} (correspond to Re = 1576 and a flow velocity of 2.36 m s^{-1}) in each single channel was chosen as the optimal operating condition for S-CFMCR and C-CFMCR.

The cycling performance of KMF02 was studied at a constant current density of 5 A g^{-1} (Fig. 6b). The specific capacitance of KMF02 electrode material was observed to be increasing continuously in the first 650 cycles and could reach ∼129.2% as
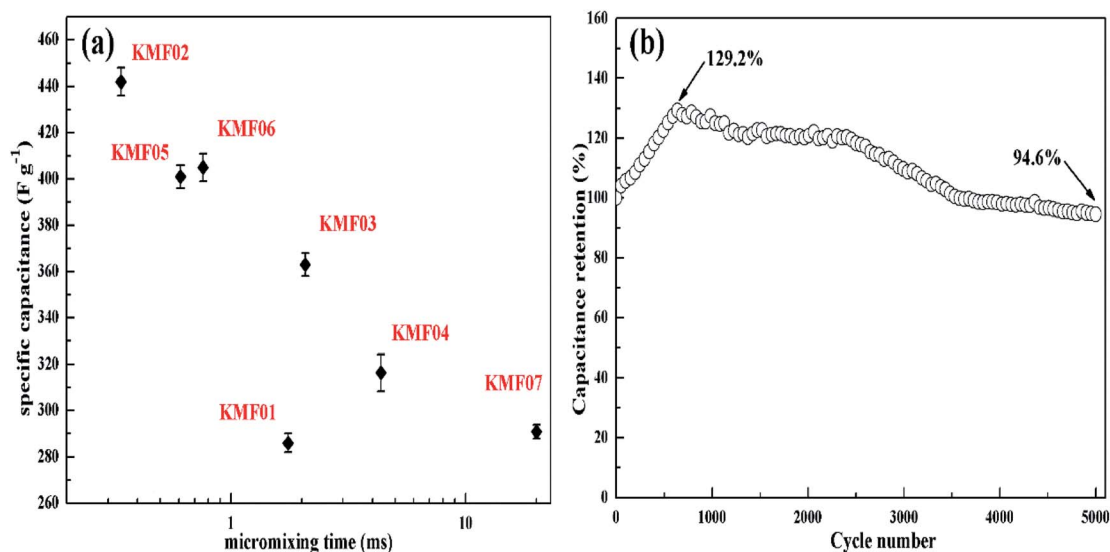

Fig. 6 (a) The specific capacitances of KMnF$_3$ prepared with different micromixing time as referred to Table 1, (b) the cycling lifetime of KMF02 at a discharge current density of 5 A g^{-1}.
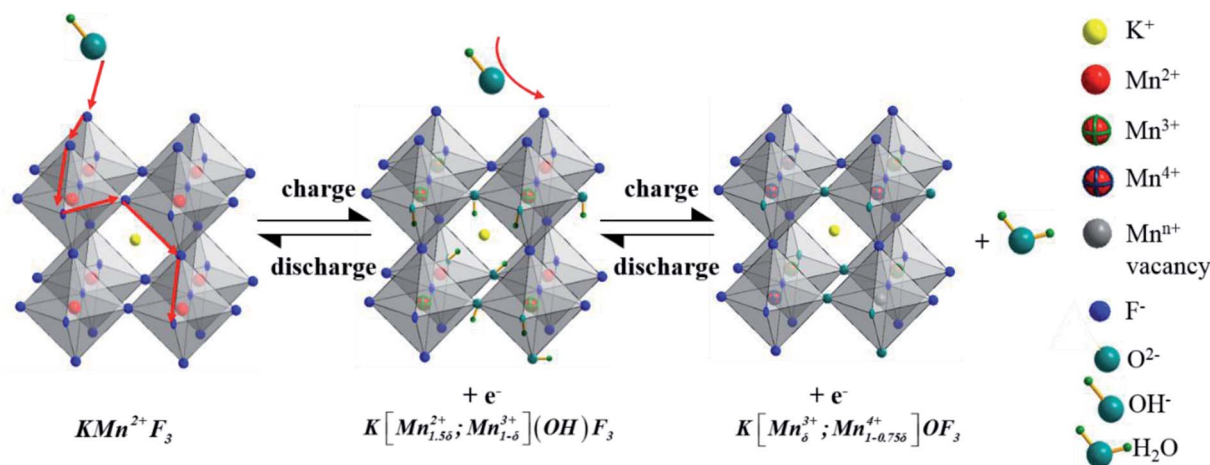

Fig. 7 Charge storage mechanism diagram of KMnF$_3$ samples.

compared with the starting cycle. It is due to the electro-activation or preconditioning of the electrodes by continuous intercalation and deintercalation of the active species on respective sites, as reported in other researchers' work.[47–50] After that, the specific capacitance decreased gradually and still retained ~94.6% of the initial specific capacitance after 5000 cycles. The dramatical decrease of specific capacitance around 2500–3500 cycles may be ascribed to the intensive increase of charge transfer resistance (Fig. 5d).

As to the charge storage of $KMnF_3$ electrode material in alkaline solution during the reversible reactions of $Mn^{2+}/Mn^{3+}/Mn^{4+}$ transition, a large amount of OH^- from electrolyte would be absorbed on the surface of electrode along with the oxidation of Mn^{2+} to Mn^{3+}. In the next step, the excessive OH^- was intercalated at the crystal surface through the diffusion of Mn^{3+} and Mn^{3+} was oxidized into Mn^{4+} to generate H_2O. The inferred mechanism of energy storage is described by the following equations (eqn (6) and (7))[21,29] and illustrated in Fig. 7.
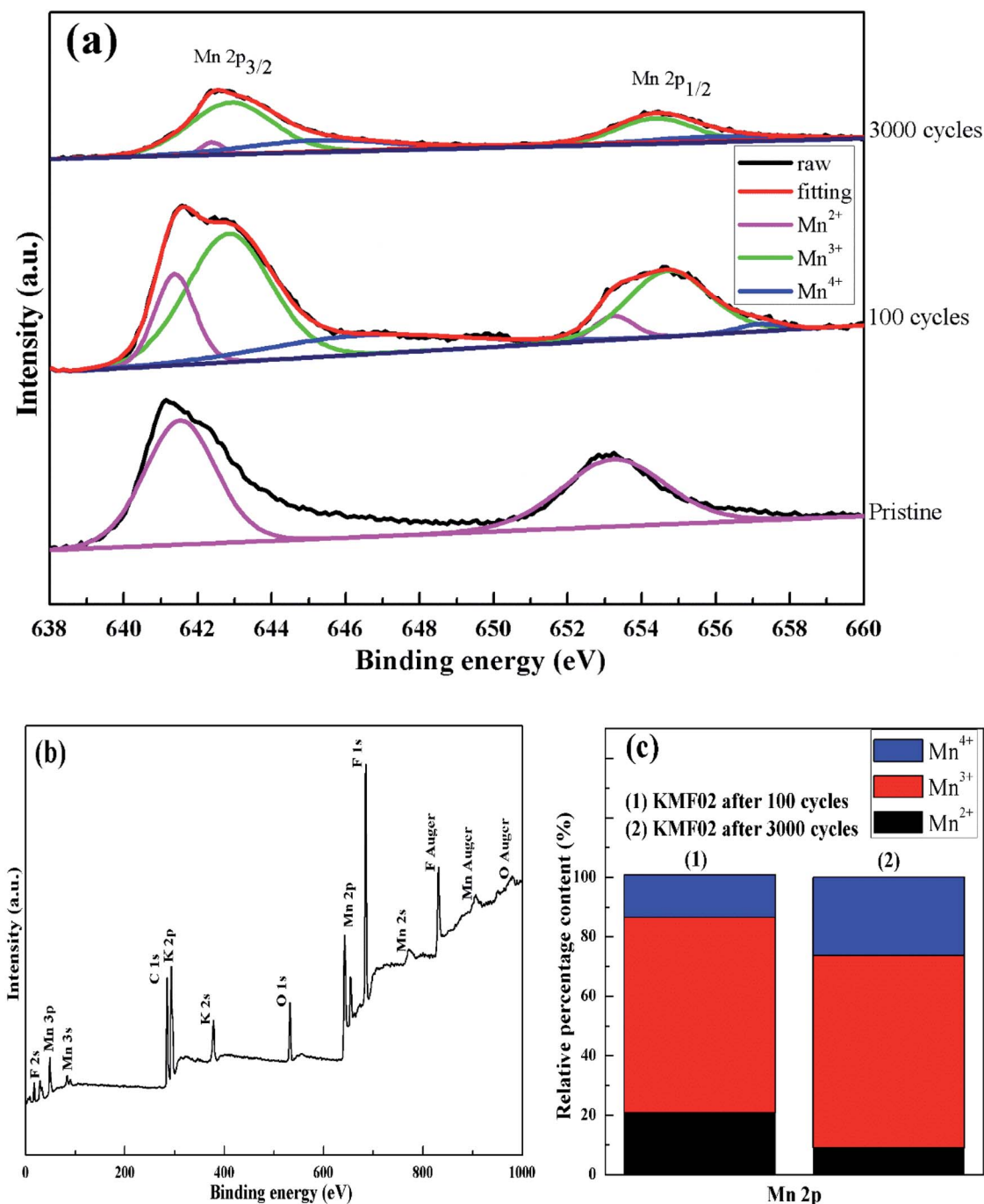

Fig. 8 XPS studies of KMF02: (a) XPS survey spectrum, (b) Mn 2p XPS spectrum of KMF02 cycled from 0–3000 times, (c) relative content of Mn species calculated from XPS spectrum.
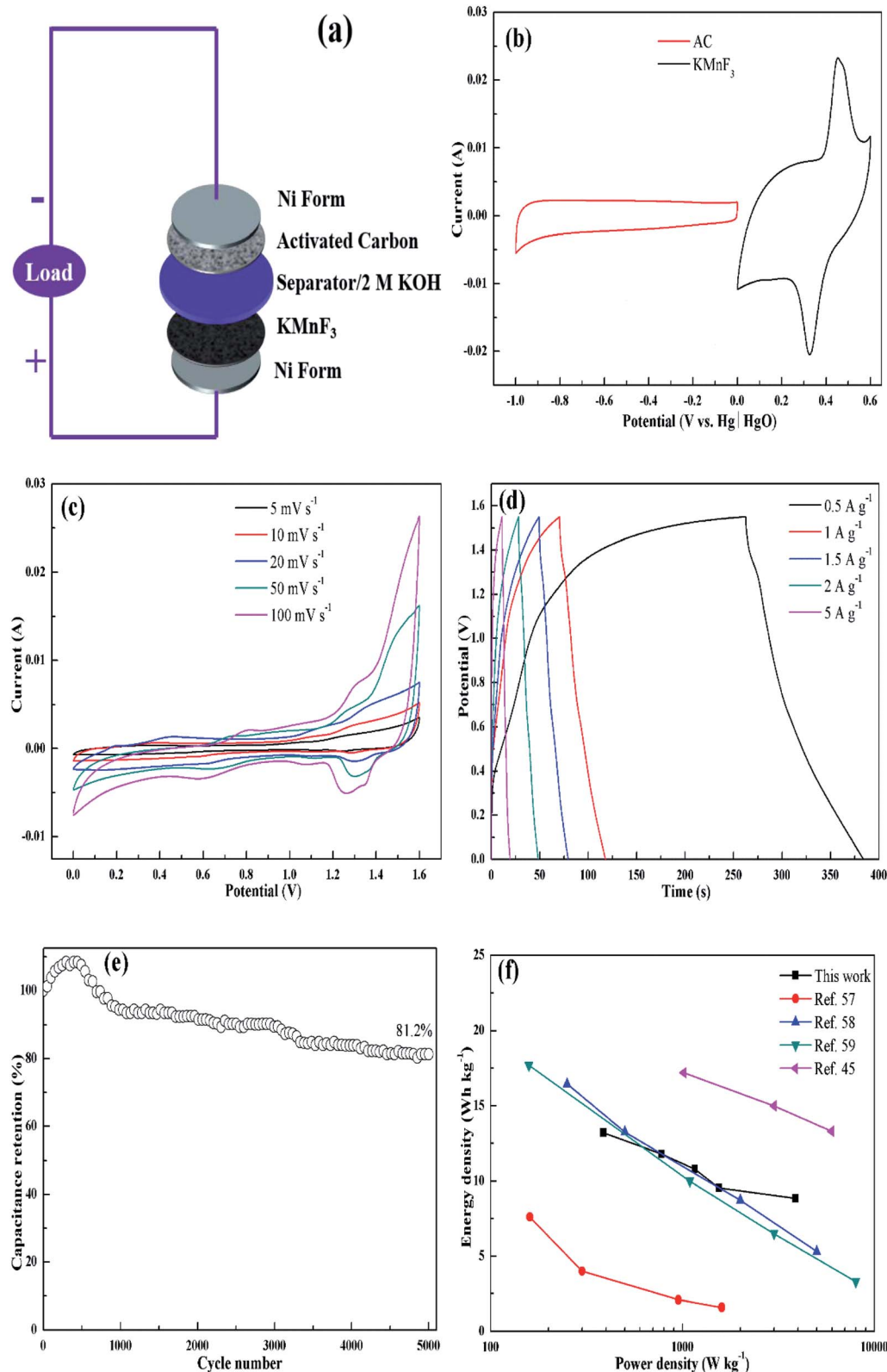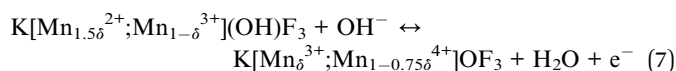
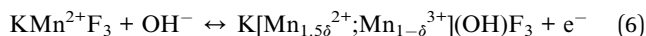Fig. 9 ASC tests: (a) schematic of the assembled asymmetric supercapacitor, (b) CV curves of KMnF$_3$ and AC at a scan rate of 10 mV s^{-1}, (c) CV and (d) GCD curves of KMnF$_3$//AC device at different scan rates and current densities, respectively, over a potential window of 0–1.55 V, (e) the cycling performance of KMnF$_3$//AC device at a current density of 1 A g^{-1}, (f) Ragone plot of the KMnF$_3$//AC device.

Paper

$$KMn^{2+}F_3 + OH^- \leftrightarrow K[Mn_{1.5\delta}^{2+};Mn_{1-\delta}^{3+}](OH)F_3 + e^- \quad (6)$$

$$K[Mn_{1.5\delta}^{2+};Mn_{1-\delta}^{3+}](OH)F_3 + OH^- \leftrightarrow$$
$$K[Mn_\delta^{3+};Mn_{1-0.75\delta}^{4+}]OF_3 + H_2O + e^- \quad (7)$$

To explore the variation of the oxidation state of manganese in the charge storage process, XPS measurement was carried out on KMF02 electrodes after 100 and 3000 cycles, respectively, and the XPS results were compared with that of the as-prepared material. Fig. 8b presents the overall XPS spectrum of the KMF02 sample at a combined energy ranging from 0 to 1000 eV, which confirmed the presence of Mn, K, and F in the as-prepared sample. The Mn 2p XPS spectrum exhibited two prominent peaks at 642.1 and 653.5 eV (Fig. 8b), which are assigned to Mn $2p_{2/3}$ and Mn $2p_{1/2}$ spin state, respectively.[45] For quantitative analysis, the peaks at 641.3 eV for Mn $2p_{2/3}$ and 652.7 eV for Mn $2p_{1/2}$ were assigned to Mn^{2+} state, the peaks at 642.7 eV and 654.4 eV were fitted to the Mn^{3+} state, and the peaks at 645.2 eV and 657.1 eV with an energy separation of 11.9 eV were typical Mn^{4+} state (Fig. 8a).[51,52] Fig. 8c presents the relative content of different state of manganese in Mn 2p spectrum of KMF02 electrodes after 100 and 3000 cycles. Compared to the state of manganese after the discharge process of 100 cycles, the content of Mn^{2+} was reduced by 11.7% and Mn^{4+} content increased by 12.0% while Mn^{3+} content remained almost unchanged after 3000 cycles, which was due to the oxidation of lower binding energy components and corresponded to the variation of valence state of manganese in Fig. 7. The significant increase of Mn^{4+} content after 3000 cycles may be responsible for the dramatic reduction of specific capacitance by weakening the electron conductivity, as reported in other publications.[53–55]

To further evaluate the practical application of the as-synthesized materials for supercapacitor, a solid-state asymmetric supercapacitor (ASC) was assembled to test its electrochemical performances, using KMF02 as positive electrode and activated carbon (AC) as negative electrode, respectively. The construction of ASC is illustrated in Fig. 9a, where 2 M KOH and nonwoven slice were employed as electrolyte and separator, respectively. Fig. 9b presents CV analyses of the negative and positive electrodes separately, showing 164 F g^{-1} of the negative electrode (AC). Hence, the calculated mass ratio of the positive and negative electrodes was 0.67 according to eqn (3). Fig. 9c gives the CV curves of the optimized ASC at various scan rates. A pair of broad redox peaks and no evident change in shape was observed with increasing scan rate, revealing fast charge–discharge ability.[56] GCD tests of the ASC at various current densities at a voltage window of 0–1.55 V are presented in Fig. 9d. Linear profile with nearly triangular symmetric shape indicated a pseudo-capacitance with good reversibility and stability. The specific capacitance of the assembled ASC was calculated through eqn (2) and found to be 39.2, 29.6, 27.2 26.5 and 22.6 F g^{-1} at the current densities of 0.5, 1, 1.5, 2 and 5 A g^{-1}, respectively. Additionally, 81.2% of the initial specific capacitance was still retained after 5000 cycles (Fig. 9e), which suggested superior stability of KMnF$_3$//AC asymmetric

supercapacitors. Meanwhile, the ACS device could deliver an energy density of 13.1 W h kg^{-1} at a power density of 386.3 W kg^{-1}. When the power density increased to 3881.0 W kg^{-1}, the device delivered a decreased energy density to 8.8 W h kg^{-1}. The performance of an ASC depends strongly on its negative electrode (activated carbon with a specific capacitance of 164 F g^{-1} was used in this work) and can be promoted with higher energy density and power density with improved negative electrodes. These results are compatible as compared to previously reported similar perovskite-like or manganese based supercapacitors.[45,57–59]

4. Conclusions

In this study, a clustered countercurrent-flow micro-channel reactor (C-CFMCR) with adjustable magnifications was assembled by numbering up its counterpart (S-CFMCR). C-CFMCRs were then employed to synthesize highly-crystallized KMnF$_3$ under varying operating conditions with different micromixing time. The prepared KMnF$_3$ was used as electrode material for supercapacitor. It was found that the micromixing time played a key role in the precipitation process and KMnF$_3$ samples obtained under close micromixing time possessed similar morphologies and electrochemical properties, and decreasing micromixing time would lead to more even size distribution as well as element distribution of the precipitates and consequently higher specific capacitance. The KMnF$_3$ particles prepared under optimal conditions displayed a specific capacitance of 442 F g^{-1} at the current densities of 1 A g^{-1} with excellent cycling stability. Moreover, the as-assembled KMnF$_3$// AC asymmetric capacitor delivered an energy density of 13.1 W h kg^{-1} at a power density of 386.3 W kg^{-1} over a wide voltage window of 0–1.55 V, and also exhibited superior lifetime with 81.2% retention of the initial specific capacitance after 5000 cycles. Additionally, the KMnF$_3$ samples prepared in S-CFMCR and C-CFMCR under optimal conditions presented superior morphology and electrochemical performance than that prepared in STR. Only a weak amplification effect of S-CFMCR to 5-times integrated C-CFMCR and 10-times assembled C-CFMCR on their application for the co-precipitation process of KMnF$_3$ was observed. These results indicated that C-CFMCR is a promising technology for the controllable and massive precipitation of nano/ultrafine materials.

Conflicts of interest

There are no conflicts of interest to declare.

Acknowledgements

References

1 L. Zhang, X. Hu, Z. Wang, F. Sun and D. G. Dorrell, *Renewable Sustainable Energy Rev.*, 2018, **81**, 1868–1878.

2 H. J. Sim, C. Choi, D. Y. Lee, H. Kim, J.-H. Yun, J. M. Kim, T. M. Kang, R. Ovalle, R. H. Baughman, C. W. Kee and S. J. Kim, *Nano Energy*, 2018, **47**, 385–392.

3 Z. Fu, Z. Li, P. Si and F. Tao, *Int. J. Hydrogen Energy*, 2019, **44**, 22146–22159.

4 Z. Bououchma, J. Sabor and H. Aitbouh, *Mater. Today: Proc.*, 2019, **13**, 688–697.

5 T. Tang, S. Cui, W. Chen, H. Hou and L. Mi, *Nanoscale*, 2019, **11**, 1728–1736.

6 B. E. Conway, *Electrochemical Supercapacitors*, Kluwer Academic/Plenum, New York, 1999, ch 2.

7 P. C. Banerjee, D. E. Lobo, R. Middag, W. K. Ng, M. E. Shaibani and M. Majumder, *ACS Appl. Mater. Interfaces*, 2015, **7**, 3655–3664.

8 Y. Wang, Y. Lu, K. Chen, S. Cui, W. Chen and L. Mi, *Electrochim. Acta*, 2018, **283**, 1087–1094.

9 X. Dong, H. Jin, R. Wang, J. Zhang and J. Lu, *Adv. Energy Mater.*, 2018, **8**, 1702695.

10 Z. Tang, C. H. Tang and H. Gong, *Adv. Funct. Mater.*, 2012, **22**, 1272–1278.

11 Z. Kai, H. Xiaopeng, H. Zhe, Z. Xiaolong and T. Zhanliang, *Chem. Soc. Rev.*, 2015, **46**, 699–728.

12 Q. Bai, Q. Xiong, C. Li, Y. Shen and H. Uyama, *Appl. Surf. Sci.*, 2018, **455**, 795–807.

13 Y. Chen, C. Chen, R. Lv, W. Shen, F. Kang, N. Tai and Z. Huang, *Chin. Chem. Lett.*, 2018, **29**, 616–619.

14 Z. Algharaibeh, X. Liu and P. G. Pickup, *J. Power Sources*, 2009, **187**, 640–643.

15 D. Ghosh and C. K. Das, *ACS Appl. Mater. Interfaces*, 2015, **7**, 1122–1131.

16 V. Khomenko, E. Raymundo-Piñero and F. Béguin, *J. Power Sources*, 2006, **153**, 183–190.

17 C. Zhu, P. Yang, D. Chao, X. Wang, X. Zhang, S. Chen, B. K. Tay, H. Huang, H. Zhang, W. Mai and H. J. Fan, *Adv. Mater.*, 2015, **27**, 4566–4571.

18 W. Wei, W. Ye, J. Wang, C. Huang, J. Xiong, H. Qiao, S. Cui, W. Chen, L. Mi and P. Yan, *ACS Appl. Mater. Interfaces*, 2019, **11**, 32269–32281.

19 Y. Liu, J. Dinh, M. O. Tade and Z. Shao, *ACS Appl. Mater. Interfaces*, 2016, **8**, 23774–23783.

20 K. Singh, R. Kannan and V. Thangadurai, *Solid State Ionics*, 2019, **339**, 114951.

21 Z. A. Elsiddig, D. Wang, H. Xu, W. Zhang, T. Zhang, P. Zhang, W. Tian, Z. Sun and J. Chen, *J. Alloys Compd.*, 2018, **740**, 148–155.

22 H.-s. Nan, X.-y. Hu and H.-w. Tian, *Mater. Sci. Semicond. Process.*, 2019, **94**, 35–50.

23 G. George, S. L. Jackson, C. Q. Luo, D. Fang, D. Luo, D. Hu, J. Wen and Z. Luo, *Ceram. Int.*, 2018, **44**, 21982–21992.

24 N. Dimov, A. Nishimura, K. Chihara, A. Kitajou, I. D. Gocheva and S. Okada, *Electrochim. Acta*, 2013, **110**, 214–220.

25 D. Cao, C. Yin, D. Shi, Z. Fu, J. Zhang and C. Li, *Adv. Funct. Mater.*, 2017, **27**, 1701130.

26 M. Wei, C. Dai, Z. Shuang, J. Yang, L. Qi and Q. Xu, *Mater. Lett.*, 2018, **27**, 66–69.

27 B. P. Hahn, J. W. Long and D. R. Rolison, *Acc. Chem. Res.*, 2013, **46**, 1181–1191.

28 M. J Tyler, W. G. Hardin, D. Sheng, K. P. Johnston and K. J. Stevenson, *Nat. Mater.*, 2014, **13**, 726–732.

29 Z. Shuang, H. Gao, Z. Cheng, Y. Jie and D. Shuai, *J. Power Sources*, 2017, **359**, 585–591.

30 Q. Tang, J. Shen, W. Zhou, J. Liu, Z. Liu and Y. Qian, *Inorg. Chem. Commun.*, 2004, **7**, 283–285.

31 S. L. Wang, W. L. Li, G. F. Wang, D. Y. Dong, J. J. Shi, X. Y. Li, P. G. Li and W. H. Tang, *Powder Diffr.*, 2013, **28**, S3–S6.

32 A. Oleaga, A. Salazar and D. Skrzypek, *J. Alloys Compd.*, 2015, **629**, 178–183.

33 H. C. Schwarzer and W. Peukert, *AIChE J.*, 2010, **50**, 3234–3247.

34 B. K. Johnson and R. K. Prud'Homme, *AIChE J.*, 2003, **49**, 2264–2282.

35 X. Shi, Y. Xiang, L. X. Wen and J. F. Chen, *Ind. Eng. Chem. Res.*, 2012, **51**, 13944–13952.

36 O. Yi, X. Yang, H. Zou, G. Chu and J. Chen, *Chem. Eng. J.*, 2017, **321**, 533–545.

37 R. Lafficher, M. Digne, F. Salvatori, M. Boualleg, D. Colson and F. Puel, *Chem. Eng. Sci.*, 2018, **175**, 343–353.

38 K.-P. Cheng, B. Wu, R.-J. Gu and L.-X. Wen, *Micromachines*, 2018, **9**, 549.

39 M. C. Fournier, L. Falk and J. Villermaux, *Chem. Eng. Sci.*, 2014, **51**, 5187–5192.

40 M. Rajkumar, C.-T. Hsu, T.-H. Wu, M.-G. Chen and C.-C. Hu, *Prog. Nat. Sci.: Mater. Int.*, 2015, **25**, 527–544.

41 Y.-S. Lin and J.-G. Duh, *J. Power Sources*, 2011, **196**, 10698–10703.

42 J. Liang, C. Wang, Y. Wang, Z. Xu, Z. Lu, Y. Ma, H. Zhu, Y. Hu, C. Xiao and X. Yi, *J. Am. Chem. Soc.*, 2016, **138**, 15829–15832.

43 I. Chung, B. Lee, J. He, R. P. H. Chang and M. G. Kanatzidis, *Nature*, 2012, **485**, 486–489.

44 J. Xu, L. Gao, J. Cao, W. Wang and Z. Chen, *Electrochim. Acta*, 2010, **56**, 732–736.

45 S. Nagamuthu, S. Vijayakumar and K. S. Ryu, *Mater. Chem. Phys.*, 2017, **199**, 543–551.

46 X. W. Wang, Q. Q. Zhu, X. E. Wang, H. C. Zhang, J. J. Zhang and L. F. Wang, *J. Alloys Compd.*, 2016, **675**, 195–200.

47 K. Y. Chen, G. J. Li, Y. J. Wang, W. H. Chen and L. W. Mi, *Green Energy Environ.*, 2020, **5**, 50–58.

48 P. M. Shafi, R. Dhanabal, A. Chithambararaj, S. Velmathi and A. C. Bose, *ACS Sustainable Chem. Eng.*, 2017, **5**, 4757–4770.

49 M. A. Bissett, I. A. Kinloch and R. A. W. Dryfe, *ACS Appl. Mater. Interfaces*, 2015, **7**, 17388–17398.

50 J. Yang, M. Ma, C. Sun, Y. Zhang, W. Huang and X. Dong, *J. Mater. Chem. A*, 2015, **3**, 1258–1264.

51 C. Zhang, C. Wang, W. Zhan, Y. Guo, Y. Guo, G. Lu, A. Baylet and A. Giroir-Fendler, *Appl. Catal., B*, 2013, **129**, 509–516.

52 Y. Chai, Z. Li, J. Wang, Z. Mo and S. Yang, *J. Alloys Compd.*, 2019, **775**, 1206–1212.

53 T. Tabari, D. Singh, A. Calisan, M. Ebadi, H. Tavakkoli and B. Caglar, *Ceram. Int.*, 2017, **17**, 15970–15977.

54 J. T. Mefford, W. G. Hardin, S. Dai, K. P. Johnston and K. J. Stevenson, *Nat. Mater.*, 2014, **13**, 726–732.

55 D. Srivastava, F. Azough, R. Freer, E. Combe, R. Funahashi, D. M. Kepaptsoglou, Q. M. Ramasse, M. Molinari, S. R. Yeandel, J. D. Baran and S. C. Parker, *J. Mater. Chem. C*, 2015, **3**, 12245–12259.

56 J. Zhang, F. Liu, J. P. Cheng and X. B. Zhang, *ACS Appl. Mater. Interfaces*, 2015, **7**, 17630–17640.

57 H. Mo, H. Nan, X. Lang, S. Liu, L. Qiao, X. Hu and H. Tian, *Ceram. Int.*, 2018, **44**, 9733–9741.

58 S. Mothkuri, S. Chakrabarti, H. Gupta, B. Padya, T. N. Rao and P. K. Jain, *Mater. Today: Proc.*, 2019, DOI: 10.1016/j.matpr.2019.03.236.

59 M. Huang, Y. Zhang, F. Li, L. Zhang, Z. Wen and Q. Liu, *J. Power Sources*, 2014, **252**, 98–106.